Photothermal wave imaging of metal-oxide-semiconductor field-effect transistor structures

Andreas Mandelis, Andrew Williams, and Edwin K. M. Siu
Photoacoustic and Photothermal Sciences Laboratory, Department of Mechanical Engineering, University of Toronto, Toronto, Ontario M5S 1A4, Canada

(Received 25 February 1987; accepted for publication 19 August 1987)

A photothermal wave imager has been assembled and used to generate thermal-wave images of an active metal-oxide-semiconductor field-effect and related inactive microelectronic structure fabricated on a silicon chip. The imager, which monitors the thermoelastic surface deformation due to absorption of a highly focused, intensity-modulated heating laser beam, has proven to be capable of producing images of subsurface features related to processing steps (thermal-wave depth profiling) at open circuit, as well as current flow sensitive images related to electronic processes in the active transistor (plasma-wave depth profiling).

I. INTRODUCTION

In recent years photothermal wave probing of solid-phase materials has developed to a fast nondestructive thermal-wave technique capable of studying microelectronic structures by use of tightly focused exciting laser beams, which yield micron-level resolution of the thermal-wave images. Of particular importance to microelectronic applications is the photothermal wave imaging instrumentation developed by Rosencwaig *et al.*[1–8] The features of that instrumentation that give it a crucial advantage over other similar imaging devices are the wideband frequency response up to several MHz and the noncontact nature of the probe (a tightly focused low-intensity probe He-Ne laser beam sampling the thermoelastic deformation gradient at the surface).

In this work a photothermal wave (PTW) imager similar in principle to that utilized by Rosencwaig *et al.*[1–8] was assembled and used to characterize *in situ* an active metal-oxide-semiconductor field effect transistor (MOSFET) and related inert microelectronic structures fabricated on a silicon chip. A conventional electrical circuit[9] was employed to power the MOSFET. The PTW images obtained from these structures demonstrated the depth-profiling abilities of our instrumentation at the integrated circuit (IC) level. They were also found to contain significant contributions from electron-hole plasma effects, as predicted by Opsal and Rosencwaig[4] and McDonald, Guidotti, and Del Giudice.[10]

II. EXPERIMENTAL RESULTS AND DISCUSSION

A. Photothermal wave imaging of inert microelectronic structures

The assembled experimental aparatus (PTW imager) is shown as a block diagram in Fig. 1. The 488-nm line of a polarized Ar^+ laser acting as the pump laser at 50–100 mW was focused on the active acoustic element of an acousto-optic (A-O) modulator through lenses L No. 1 and L No. 2. The diffracted first-order beam was modulated by a sinewave generator at a chosen frequency and was further separated from the zeroth-order beam using a knife edge. The 3× expanded beam was then passed through a He-Ne dichroic mirror and eventually was reflected into the pupil of a 50× microscope objective. The output beam diameter at the focal plane was $\sim 3\,\mu$m and was focused onto the sample surface. Wafer samples can be positioned on a manually scanned sample holder with submicrometer translation capabilities in the x and y directions of the focal plane. The probe beam was a 4-mW 632.8-nm line of a plane polarized He-Ne laser. The 3× expanded beam was passed through a polarizing beamsplitter and a quarter-wave plate. The emerging circularly polarized beam was essentially totally reflected by the dichroic mirror and then traveled collinear to the pump beam. In fact, the relative position of the axes of the two propagating beams can be varied ("tuning" of the imager) so as to give a maximum signal. The maximum signal results from the angular deflection of the probe beam from the steepest gradient of the thermoelastic deformation produced locally in the pump beam-heated region of a sample.[2] The separation of pump and probe beams was $\sim 1.8\,\mu$m in our experiments. The tightly focused ($\leqslant 5\,\mu$m) circularly polarized direct probe beam is thermoelastically deflected at the pump beam modulation frequency and then reflected

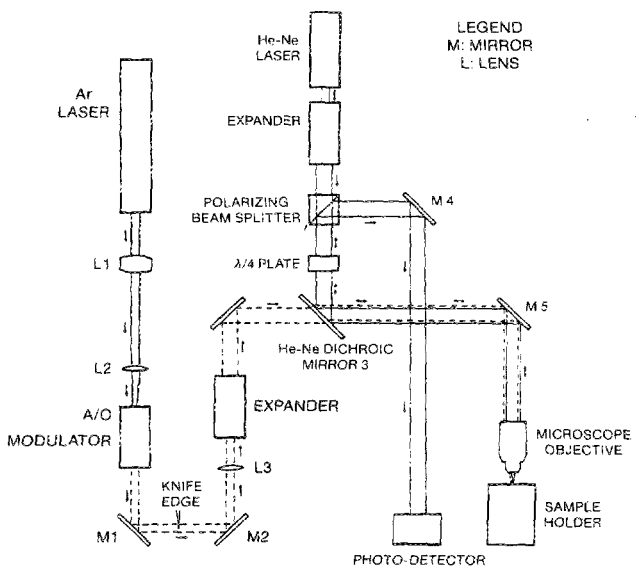

FIG. 1. Schematic diagram of PTW Imager apparatus. The entire assembly rests on an antivibrational optical table.

 0021-8979/88/010092-07$02.40 © 1987 American Institute of Physics

Downloaded 18 Jul 2008 to 128.100.49.17. Redistribution subject to AIP license or copyright; see http://jap.aip.org/jap/copyright.jsp

with the circular polarization rotating in the opposite (mirror image) sense. As it travels back, approximately retracing its path toward the He-Ne laser, it becomes plane polarized after passage through the $\lambda/4$ plate, with its field vectors orthogonal to those of the direct beam. It is then reflected by the polarizing beamsplitter and filtered into a bi-cell photodetector whose normalized output is proportional to the beam deflection magnitude. The signal (amplitude and phase) is recovered using a combination of high- and low-frequency lock-in analyzers. Depending on the pump beam modulation frequency f, Opsal, Rosencwaig, and Willenborg[2] have shown that the amplitude of the ac thermoelastic deflection profile, $\delta_2(r)$, in the probed solid, at a radial distance r from the center of the heating beam, is proportional to an integral of the type

$$\left| \int F(x)\, J_1\left(\frac{rx}{L_s}\right) \exp\left(\frac{-a^2x^2}{4L_s^2}\right) dx \right| , \tag{1}$$

where a is the radius of the (assumed Gaussian) pump beam, $F(x)$ is a function depending on x only, J_1 is the cylindrical Bessel function of first order, and L_s is the thermal diffusion length in the material given by

$$L_s(f) = (\alpha_s/\pi f)^{1/2} , \tag{2}$$

where α_s is the sample thermal diffusivity. The form of (1) shows that significant contributions to the photothermal wave signal can essentially be made from characteristic depths in the material such that

$$L_s(f) \leqslant a/2, \tag{3}$$

due to the rapid decay of the exponential in the above integrand (1). Relation (3) is in agreement with numerical results (Ref. 2, Fig. 3) and shows that thermal information can be obtained from shallower layers in the case of more highly focused pump beams. If different sample regions are scanned, any variations in α_s, will affect the value of L_s and thus will register as signal changes according to (1). This results in photothermal mapping of surface and subsurface regions with different thermal properties. The modulation frequency f is used as a control parameter governing depth resolution and profiling. Lateral resolution is determined by the width of the pump beam at the sample surface and the thermal diffusion length in the material as shown by Opsal and co-workers[2]:

$$\delta_2(r) \propto \frac{1}{L_s} \left| \int x^2\, dx\, \frac{J_1(rx/L_s)\exp(-a^2x^2/4L_s^2)}{\sqrt{x^2-2i}(x+\sqrt{x^2-2i})} \right| \tag{4}$$

assuming an infinitesimal probe beam radius. For finite probe beam radii, a convolution integral over the spatial extent of the probe-illuminated area will render the photothermal wave signal (and the lateral resolution) dependent on the probe radius width.

A silicon chip with a MOSFET and other related structures was mounted onto the focal plane of the imager and the usual power circuit and detection electronics was built around it. The drain current-voltage characteristics of the transistor were found to be in good agreement with typical curves of such devices[9] and are shown in Fig. 2. A magnified view of the device is shown in Fig. 3. In that figure the out-of-focus structures are wires. The marked region on Fig. 3 is the

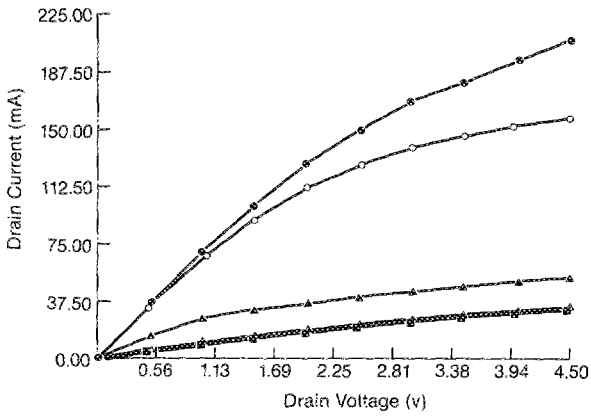

FIG. 2. Drain current (I_D) vs drain voltage (V_D) of a MOSFET with the source-gate applied voltage (V_G) as a parameter. ■-■: $V_G = 0.05$ V; Δ-Δ: $V_G = 0.5$ V; ▲-▲: $V_G = 1.5$ V; O-O: $V_G = 2.5$ V; ●-●: $V_G = 3.5$ V.

one selected for scanning as discussed below. Figure 4 shows the PTW imager frequency response sampled at the gate of the MOSFET. The thermoelastic deformation probing gave good, nearly flat responses and strong signals between 10^2 and 10^5 Hz; signal strength also increases above 1 MHz as shown in Fig. 4. This extended high-frequency behavior is consistent with previous measurements[2] and gives depth resolution capability better than 2–3 μm at 1 MHz in Si, using the criterion of Eq. (3) with $\alpha_{Si} = 1.06$ cm^2/s.[11] The observed higher signal regularity of phase response than that of thermal-wave amplitude was found to be characteristic of the generally higher-quality phase data throughout our entire set of experiments. This observation has not been appreciated in the previous literature on the thermoelastic deformation imaging to the best of our knowledge.[2,12]

The flat frequency response at modulation frequencies $\leqslant$ 100 kHz exhibited by the amplitude data of Fig. 4 in this work is in agreement with theoretical considerations of the frequency dependence of the probe beam deflection leading to Fig. 4 in Ref. 2. According to the Opsal–Rosencwaig (O–R) model[12] and its 3-D extension[2] leading to relation (3),

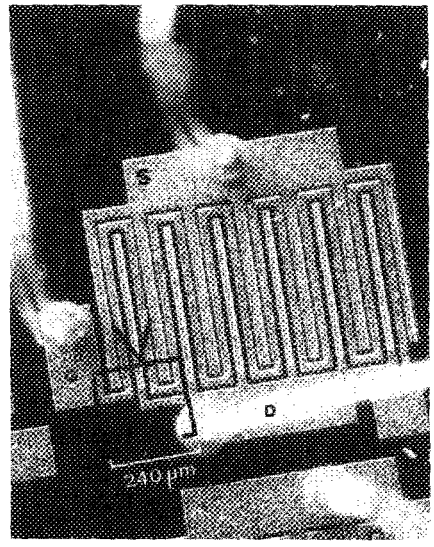

FIG. 3. Magnified view of the MOSFET, including scanned regions. S = source; G = gate; D = drain.

Downloaded 18 Jul 2008 to 128.100.49.17. Redistribution subject to AIP license or copyright; see http://jap.aip.org/jap/copyright.jsp

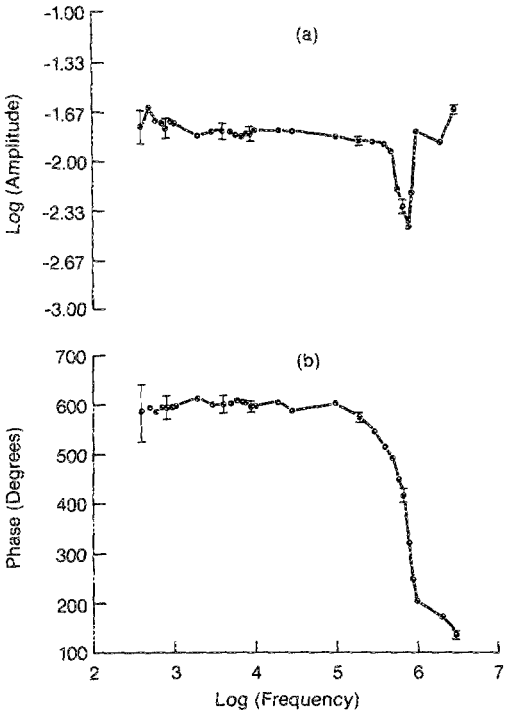

FIG. 4. PTW imager frequency response from the gate region of the MOSFET; (a) amplitude, and (b) phase. Error bars are indicated every five data points.

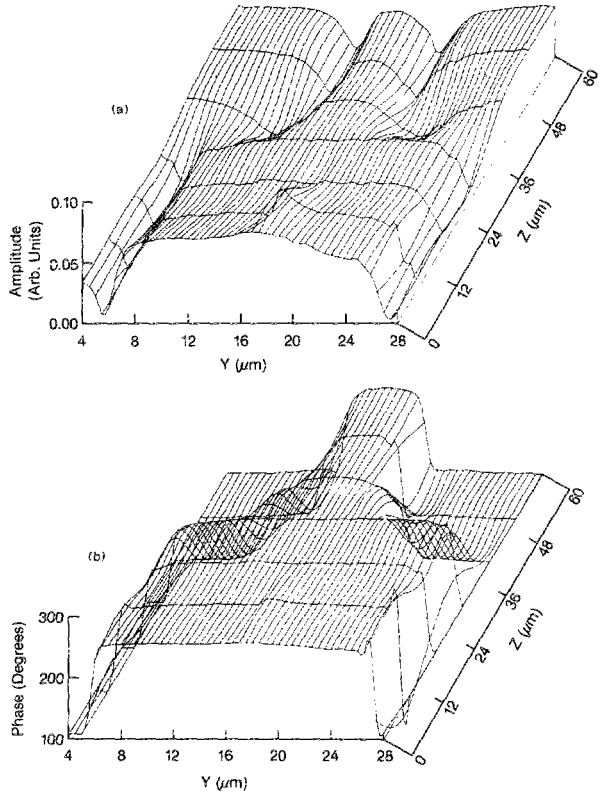

FIG. 5 Thermal-wave scan of a MOSFET gate metal padding as it narrows into the gate strip (Fig. 3). Light modulation frequency: 1 MHz; (a) amplitude, and (b) phase.

the probe beam deflection should become independent of f as $f \to 0$ and for modulation frequencies such that $a/L_s(f) < 1$, where a is the focused beam radius. Using $a \approx 3\ \mu$m for our experiments, the condition for frequency-independent deflections becomes valid at $f < 1$ MHz, in agreement with Fig. 4. The amplitude rise above 1 MHz and the associated large phase shift in Fig. 4 are not well understood at present, however, these trends are consistent with the increased amplitude of the modulated reflectance of a thin layer on top of crystalline silicon, in which two interfering thermal waves from a thin metallic film (gate) and the substrate are contributing to the signal.[13]

The different nature of phase imaging from that of the amplitude image can be seen in the thermal-wave scans of Fig. 5. With pump and probe laser beam sizes $\sim 3\ \mu$m, the metal padding interconnected to the gate interdigital electrode of a MOSFET on the silicon chip was scanned in the neighborhood of the region where the padding narrows into the size of the gate metal strip ($\sim 5\ \mu$m width, Fig. 3). Once the detector signal was maximized, the slightly ($\approx 1.8\ \mu$m) separated pump and probe beams were scanned across the structure at 0.5-μm steps. Figure 5 shows the thermal-wave image components (amplitude and phase) at 1 MHz. It can be seen that the lateral contrast (defined as the minimum signal-level difference between two different adjacent materials such as silicon and metal in Fig. 5) which is afforded by the phase image is of higher quality than the amplitude image. This point was further appreciated from individual single line scans of the narrow ($5\ \mu$m) gate interdigital metallization, which make up Fig. 5. The level contrast was much sharper in the phase plots than in the amplitude plots. The discontinuity points in crossing from one surface (metal) to the next (silicon) were seen to cause signal distortions, which are spatially farther extended in the amplitude than in the phase scan. At this time a tentative explanation of the edge distortions is given in terms of edge effects of the exciting laser beam as it partially overlaps two different material regions in space, similar in nature to those observed previously photoacoustically.[14,15]

Depth-profiling characteristics (depth resolution) were also tested using a test metallization on the chip of Fig. 3. Surface scans were performed at various modulation frequencies, as shown in Fig. 6. Images were thus obtained with 1 kHz, 50 kHz, and 1 MHz modulation frequency in crossing the metal-silicon interface. From Fig. 6 it is apparent that the high contrast of the phase signal between the two regions at 1 MHz rapidly deteriorates with decreasing frequency below 100 kHz. A high contrast in the amplitude signal, however, is present down to 1 kHz. It is well-known[16] that photothermal wave amplitudes carry information from the sample reflectivity in the form $[1 - R(\lambda)]$, whereas phases being the ratio of two signals are independent of $R(\lambda)$. Figure 6 is a manifestation of this fact and it shows that the reflectivity variation across the scan line is the predominant factor in the thermal-wave amplitude. It thus appears that the phase should be the preferred information channel, as it depends on thermal properties only and, therefore, gives true thermal wave images. In this case, amplitude images are dominated by optical effects and thus resemble optical images. Similar conclusions were arrived at by Rosencwaig and Busse,[17] for the piezoelectric photoacoustic detection tech-

Downloaded 18 Jul 2008 to 128.100.49.17. Redistribution subject to AIP license or copyright; see http://jap.aip.org/jap/copyright.jsp

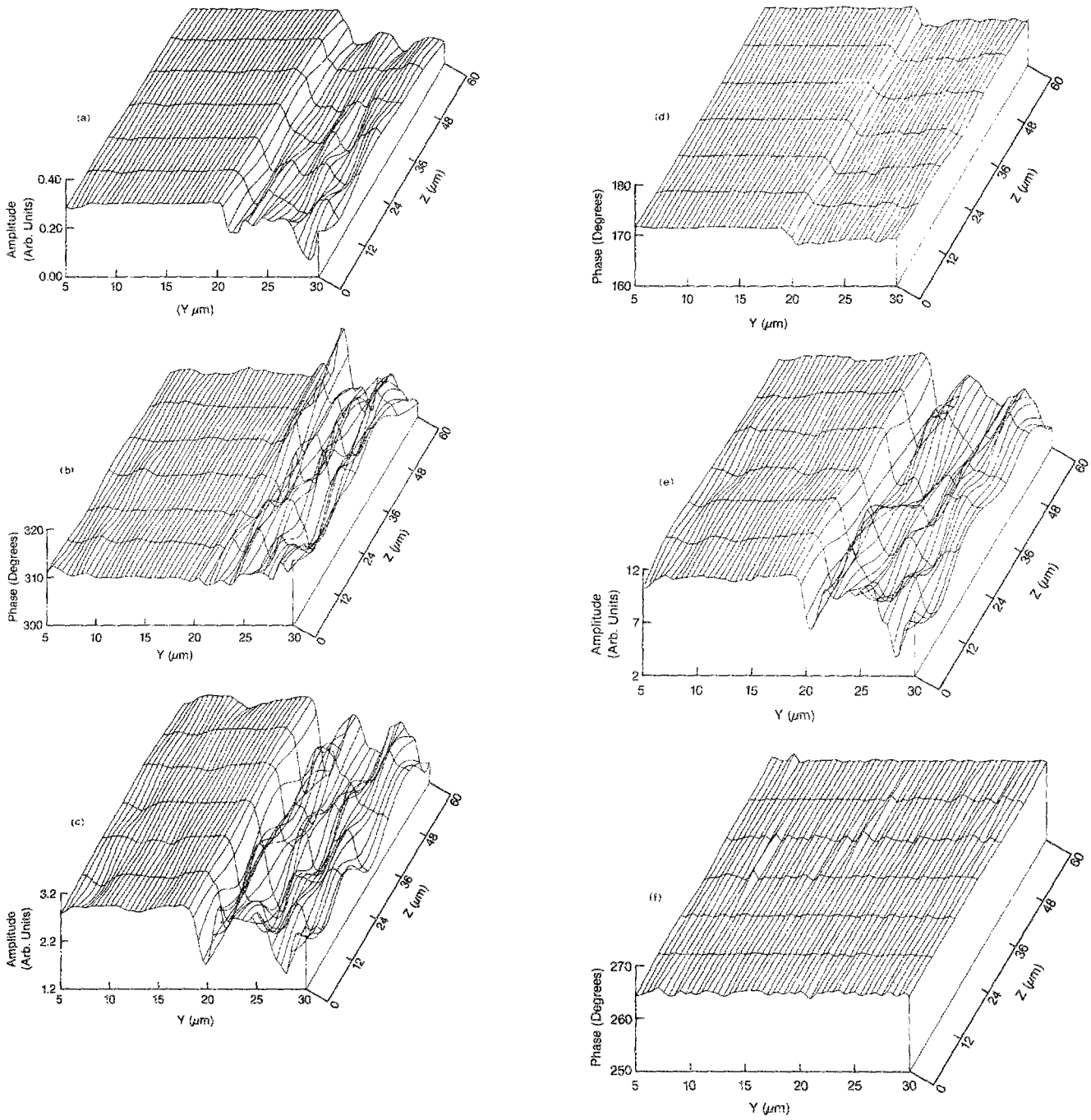

FIG. 6. Thermal-wave images of metal-silicon interface of test structure on the silicon chip. (A): amplitude; (P): phase. Modulation frequencies: (a) 1 MHz (A); (b) 1 MHz (P); (c) 50 kHz (A); (d) 50 kHz (P); (e) 1 kHz (A); (f) 1 kHz (P). The metallization region lies on the right side of the images.

nique. An important conclusion of this particular experiment is that phase contrast for shallow microelectronic structures on silicon substrates is strong, but measurable only at high frequencies on the order of 1 MHz: At low frequencies the thermal diffusion length L_s is dominated by thermal contributions from the much thicker silicon substrate whose thermal properties are the same as those of the surrounding material. Therefore, at those lower frequencies there is little or no thermal difference between metal and surrounding silicon and the phase contrast is lost. At 1 kHz, the thermal diffusion length in silicon is $\sim 180\ \mu$m, so that the presence of the ~ 2-μm-thick metallization on the surface contributes insignificantly to the thermal-wave signal. As a result, the phase suffers complete lack of contrast at 1 kHz. It is interesting to note the phase variations across the metallization region. These are true thermal effects and may be due to metal thickness differences locally, or, more likely due to poor physical contact with the substrate, which would introduce a variable thermal resistance at the back interface.

The different structure of amplitude and phase images of the MOSFET padding in Fig. 5 can also be explained in terms of the reflectivity contribution to the former image, as opposed to the true thermal-wave image generated by the phase channel. Thus, the amplitude channel data are complicated by optical effects and of poorer contrast than the phase.

Downloaded 18 Jul 2008 to 128.100.49.17. Redistribution subject to AIP license or copyright; see http://jap.aip.org/jap/copyright.jsp

B. Photothermal wave imaging of the active MOSFET device

Figure 7 is the thermal-wave image of the marked area in Fig. 3 at 1.02 MHz, with the MOSFET inactive at open circuit. It can be seen from Figs. 7(a) and 7(b) that the various electrodes of the interdigital structure D-G-D-S-G can be well resolved in both amplitude and phase components of the signal, however, for reasons discussed in Sec. II A, only the phase image should be considered a true thermal-wave image. Figures 7(c) and 7(d) are isometric contour maps of Figs. 7(a) and 7(b) generated by use of a FORTRAN routine which interconnects signal levels of equal magnitudes ("isometric"). Increasing numbers in the isometric contours represent higher amplitude signal or greater phase lag. The amplitude contour map clearly identifies all interdigital electrodes with the phase map bearing close resemblance to it. With the circuit connected, the pump/probe beam system was focused on the drain and the thermal-wave signal was recorded as a function of V_D for various levels of V_G and the source grounded. Figure 2 indicates that within the experimental V_D range $0\ \text{V} \leqslant V_D \leqslant 4.5\ \text{V}$, the $(V_D)_{\text{saturation}}$ onset is evident, however, complete saturation has not occurred. Figure 8 shows the resulting thermal-wave signals as functions of V_D. The single datum labeled "a" at $V_D = 0$ V is the reading taken at open circuit. The single datum labeled "b" is the reading of the background signal at $V_D = 0$ V with the pump beam blocked. Both these points are useful reference data. Two trends are apparent in Fig. 8: the thermal wave signal *decreases* with *increasing* V_D at constant V_G; and it *increases* with *decreasing* V_G at constant V_D. This behavior can be explained, at least qualitatively, in terms of the electron/hole plasma-wave contribution to the photothermal signal.[4] Optical excitation at 488 nm with no applied V_D leads to nonradiative recombination of photogenerated electron/hole pairs, and the released heat affects the thermal-wave signal. When $V_D > 0$ V some of the otherwise spatially confined carriers will roll into the external circuit as current whose magnitude increases with increasing V_D (Fig. 2). Therefore (assuming negligible luminescence), not all the plasma energy will be deposited nonradiatively in the lattice and, as a result, the thermal-wave signal will diminish with increased V_D (Fig. 8). Furthermore, for a given constant $V_D > 0$ V and constant V_s (usually grounded source), decreasing V_G decreases the conductance of the conducting-surface channel under the oxide beneath the electrode and thus enhances the recombination probability of electron/hole pairs resulting in an increased thermal wave signal (Fig. 8) and a decreased current magnitude (Fig. 2).

The image of the active MOSFET with $V_D = V_G = 1.5$ V is shown in Fig. 9. When compared with Figs. 7(a) and 7(b) this image exhibits lower contrast between each scanned electrode and the surrounding substrate in both amplitude [Fig. 9(a)] and phase [Fig. 9(b)] mode in agreement with trends shown in Fig. 8. In the light of the above discussion it transpires that the PTW imager may be used as a plasma-wave imaging instrument beyond its thermal-wave imaging capabilities.

The MOSFET depth-profiling capability of our imager was tested by scanning the structure of the marked region of

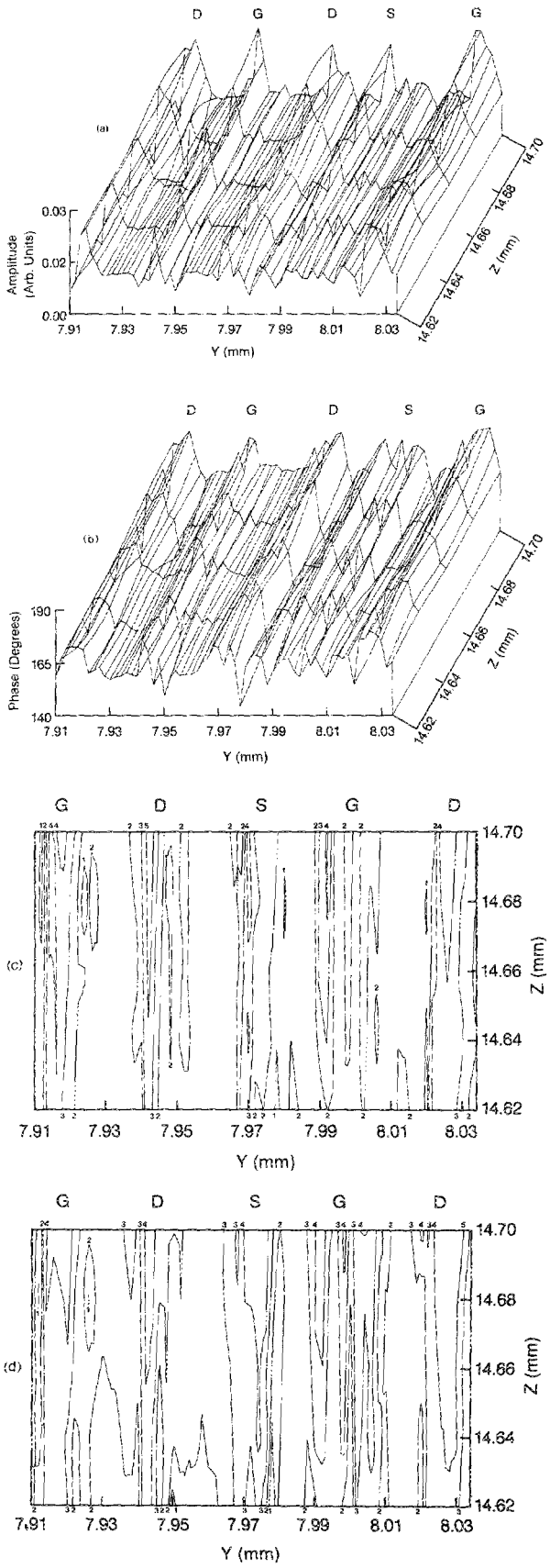

FIG. 7. Thermal-wave image of interdigital components of the MOSFET of Fig. 3 at open circuit; $f = 1.02$ MHz; (a) amplitude; (b) phase; (c) isometric contour map of amplitude with numbers corresponding to height (intensity of signal) in arbitrary units. (1) 0.0096, (2) 0.0136, (3) 0.0177, (4) 0.0218, and (5) 0.0259; (d) isometric contour map of phase with numbers corresponding to degrees. (1) 153.17°, (2) 161.90°, (3) 170.63°, (4) 179.37°, and (5) 188.10°.

Downloaded 18 Jul 2008 to 128.100.49.17. Redistribution subject to AIP license or copyright; see http://jap.aip.org/jap/copyright.jsp

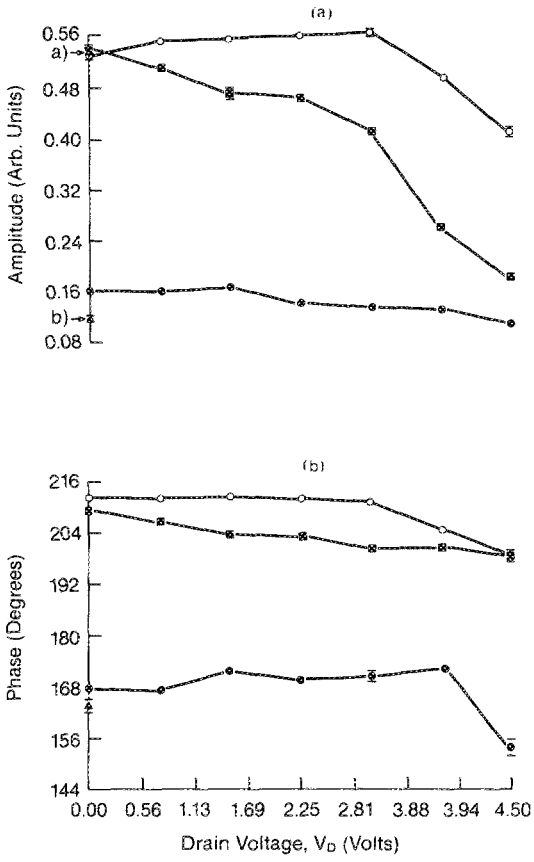

FIG. 8. Thermal-wave signal vs drain voltage (V_D) with gate voltage (V_G) as a parameter; $f = 1$ MHz; (a) amplitude, and (b) phase. O-O: $V_G = 0.05$ V; ▩-▩: $V_G = 1.5$ V; ⊛-⊛: $V_G = 3.5$ V.

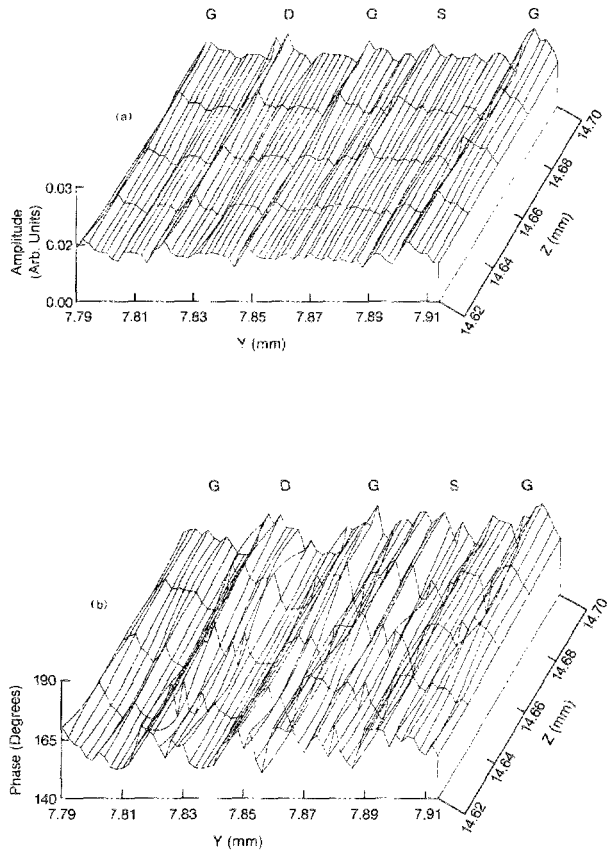

FIG. 9. Thermal-wave image of active MOSFET at 1 MHz with $V_G = V_D = 1.5$ V: (a) amplitude, and (b) phase.

Fig. 3 at 10 kHz. The results are shown in Fig. 10. Figure 10(a) is the amplitude image and is quite similar to Fig. 7(a) because of optical contributions to the signal, as discussed in Sec. II A. The phase image [Fig. 10(b)] however, is a truly thermal-wave image and entirely different from Fig. 7(b): substantial subsurface contributions to the phase signal from the active implanted channels, which form the source and drain in the device, are shown very clearly and with a high degree of regularity. Figure 10(d) indicates the buried structure in the isometric contour map representation and identifies regions of largest doping levels. The 10-kHz modulation frequency corresponds to an $L_s \approx 10$ μm, which encompasses the $\sim$5–10-μm-deep buried structures and channels of the MOSFET. The contour map of Fig. 10(e) shows, by comparison, the change in subsurface features of Fig. 10(d) due to the plasma-wave contribution in the activated device. It appears that a defect structure, which is evident in the S region of Fig. 10(a) through a local maximum ("hill") in the thermal-wave signal, is an efficient recombination source [region marked 5 in Fig. 10(e)] in the activated device giving a local maximum contour. A more detailed analysis of the extent of subsurface features and plasma-wave related contributions to the signal[18] will be necessary to understand quantitatively the combined thermal- and plasma-wave images obtained from the activated MOSFET.

III. CONCLUSIONS

In this work it has been shown that *inactive* microelectronic device-level geometries can give high-quality contrast thermal-wave images through the phase channel of a PTW imager operating on the principle of thermoelastic deformation, provided experiments are performed in the MHz range of modulation frequencies. In that range sensitivity to shallow subsurface geometries increases, as the thermal diffusion length becomes comparable to the thickness of various device structures (ca. a few microns).

Further, it has been demonstrated that *active* microelectronic devices can be probed with the PTW imager and, in the case of MOSFETs, the thermal wave signal can yield subsurface structure information related to device fabrication. We have also showed that *in situ* electron/hole plasma-wave imaging is feasible with many exciting possibilities in the areas of microelectronic industrial process control and fundamental solid-state device physics.

Downloaded 18 Jul 2008 to 128.100.49.17. Redistribution subject to AIP license or copyright; see http://jap.aip.org/jap/copyright.jsp

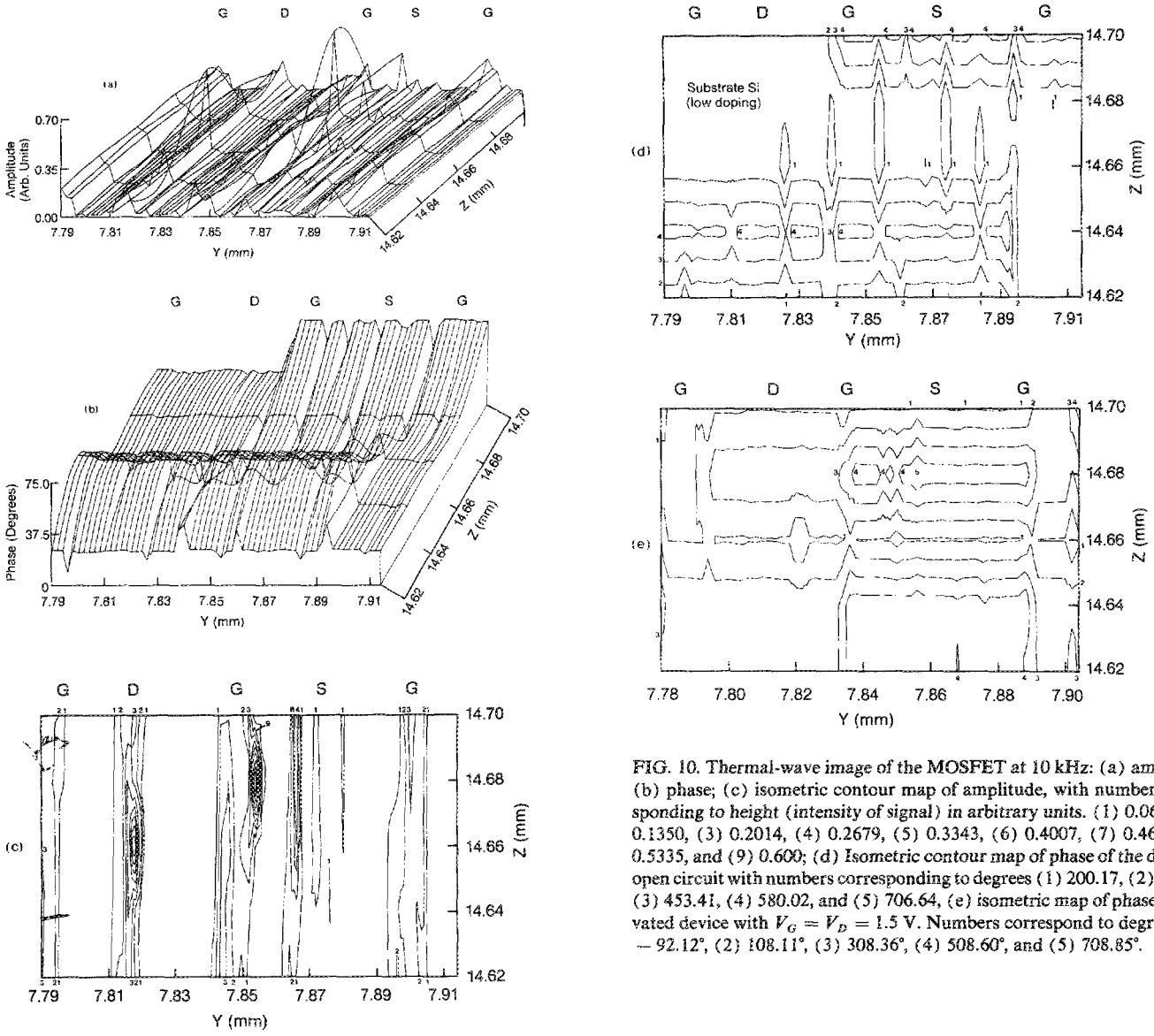

FIG. 10. Thermal-wave image of the MOSFET at 10 kHz: (a) amplitude; (b) phase; (c) isometric contour map of amplitude, with numbers corresponding to height (intensity of signal) in arbitrary units. (1) 0.0686, (2) 0.1350, (3) 0.2014, (4) 0.2679, (5) 0.3343, (6) 0.4007, (7) 0.4671, (8) 0.5335, and (9) 0.600; (d) Isometric contour map of phase of the device at open circuit with numbers corresponding to degrees (1) 200.17, (2) 326.79, (3) 453.41, (4) 580.02, and (5) 706.64, (e) isometric map of phase of activated device with $V_G = V_D = 1.5$ V. Numbers correspond to degrees. (1) $-92.12°$, (2) 108.11°, (3) 308.36°, (4) 508.60°, and (5) 708.85°.

ACKNOWLEDGMENTS

The authors wish to express their gratitude to the National Sciences and Engineering Research Council of Canada for support of this work through a University-Industry grant (A.M. and E.K.M.S.) and a summer research grant (A.W.). The donation of the silicon chip containing the MOSFET by Dr. C.A.T. Salama of the VLSI Laboratory, Dept. of Electrical Engineering, University of Toronto, is also gratefully acknowledged. It is a pleasure to further acknowledge many enlightening discussions with Johnny Sin of the VLSI Laboratory.

[1]A. Rosencwaig, J. Opsal, and D. L. Willenborg, J. Phys. (Paris) Colloq. **44**, C6-483 (1983).
[2]J. Opsal, A. Rosencwaig, and D. L. Willenborg, Appl. Opt. **22**, 3169 (1983).
[3]A. Rosencwaig, J. Photoacoust. **1**, 371 (1982-83).
[4]J. Opsal and A. Rosencwaig, Appl. Phys. Lett. **47**, 498 (1985).
[5]A. Rosencwaig, J. Opsal, W. L. Smith, and D. L. Willenborg, Appl. Phys. Lett. **46**, 1013 (1985).
[6]W. L. Smith, A. Rosencwaig, and D. L. Willenborg, Appl. Phys. Lett. **47**, 584 (1985).
[7]A. Rosencwaig, J. Opsal, W. L. Smith, and D. L. Willenborg, J. Appl. Phys. **59**, 1392 (1986).
[8]J. Opsal, M. W. Taylor, W. L. Smith, and A. Rosencwaig, J. Appl. Phys. **61**, 240 (1987).
[9]S. M. Sze, *Physics of Semiconductor Devices* (Wiley, New York, 1969), Chap. 10.
[10]F. A. McDonald, D. Guidotti, and T. M. Del Giudice, IBM Research Report RC 12121 (#54561) (1986).
[11]Y. S. Touloukian, R. W. Powell, C. Y. Ho, and M. C. Nicolaou, in *Thermal Diffusivity* (IFI/Plenum, New York, 1973).
[12]J. Opsal and A. Rosencwaig, J. Appl. Phys. **53**, 4240 (1982).
[13]A. Rosencwaig, J. Opsal, and D. L. Willenborg, Appl. Phys. Lett. **43**, 166 (1983).
[14]J. F. McClelland and R. N. Kniseley, Appl. Phys. Lett. **35**, 585 (1979).
[15]R. A. McFarlane and L. D. Hess, Appl. Phys. Lett. **36**, 137 (1980).
[16]A. Mandelis, E. K. M. Siu, and S. Ho, Appl. Phys. A **33**, 153 (1984).
[17]A. Rosencwaig and G. Busse, Appl. Phys. Lett. **36**, 137 (1980).
[18]J. Opsal and A. Rosencwaig, Appl. Phys. Lett. **47**, 498 (1985).

Downloaded 18 Jul 2008 to 128.100.49.17. Redistribution subject to AIP license or copyright; see http://jap.aip.org/jap/copyright.jsp